

Moderate Gilbert damping and perpendicular magnetic anisotropy in Yb₃Fe₅O₁₂ filmsKishori Lal¹,¹ Manik Kuila¹,¹ B. Samantaray¹,¹ R. J. Choudhary,² V. Raghavendra Reddy^{1,2}, and Z. Hossain^{1,*}¹*Department of Physics, Indian Institute of Technology Kanpur, Kanpur 208016, India*²*UGC-DAE Consortium for Scientific Research, Khandwa Road, Indore 452017, India*

(Received 21 November 2023; revised 4 March 2024; accepted 1 April 2024; published 3 May 2024)

The realization of perpendicular magnetic anisotropy (PMA) in a rare-earth iron garnet composition has the potential to open up the field of spintronics and magnonics. In this study, we introduce Yb₃Fe₅O₁₂ (YbIG) as an iron garnet thin film candidate exhibiting PMA. We have grown highly epitaxial YbIG films on (111) oriented Gd₃Ga₅O₁₂ (GGG) substrates. Detailed growth, structural, magnetic, and dynamical properties of the YbIG/GGG(111) thin films are reported. We reveal a transition from the in-plane (IP) to out-of-plane (OOP) magnetic easy-axis as the film thickness decreases. The gradual increase in the OOP anisotropy field from 18 Oe to 1100 Oe with decreasing film thickness is consistent with the observed variation of the OOP lattice parameter due to epitaxial strain. Further, sixfold symmetry in the IP angular variation of resonance field H_r reveals the presence of a significant contribution of the second-order magnetocrystalline anisotropy (K_2). The damping factor $\alpha \sim 10^{-2}$ is comparable to TmIG, which has been proposed as a promising material for application due to PMA. These findings present YbIG as a potential contender for spintronic and magnonic applications because of its PMA with moderate α .

DOI: [10.1103/PhysRevB.109.184406](https://doi.org/10.1103/PhysRevB.109.184406)**I. INTRODUCTION**

Ferrimagnetic insulators offer a wealth of opportunities for uncovering spintronics-related effects, such as the spin Seebeck effect [1], spin Hall magnetoresistance [2], spin pumping [3], anomalous Hall effect [4], and the inverse spin Hall effect [5] etc. Additionally, it has been demonstrated to be a fascinating medium for pure spin current lasting over extended distances due to its insulating characteristics [6]. Among ferrimagnetic insulators, rare earth iron garnets (REIGs) stand out for their unique properties and potential for practical applications. Since the past decade, researchers have shown a great deal of interest in REIG films with perpendicular magnetic anisotropy (PMA). The presence of PMA in REIG films open up exciting possibilities for the development of novel applications and mechanisms, including spin-orbit torques [7], the Rashba-Edelstein effect [8], as well as logic and racetrack memory devices [9]. Furthermore, devices utilizing PMA films offer the advantages of compact size, enhanced speed, higher thermal stability, and improved efficiency.

REIG thin films with PMA have been explored by various groups for different phenomena and properties, i.e., Dy₃Fe₅O₁₂(DyIG) [10], Bi₃Fe₅O₁₂(BiG) [11], Eu₃Fe₅O₁₂(EuIG) [12], Sm₃Fe₅O₁₂(SmIG) [13], and Tm₃Fe₅O₁₂(TmIG) [14,15] etc. TmIG and EuIG are the garnets with robust PMA and explored vastly for spin-related phenomena and applications [16–20]. Zanjani *et al.* theoretically identified Yb₃Fe₅O₁₂(YbIG) as a potential PMA candidate [21]. Yb³⁺ ion is one electron less for having a closed 4*f* electron shell (4*f*¹³) with ground state ²F_{7/2}. Tm³⁺ ion has configuration 4*f*¹², which lead to stronger

spin-orbit coupling and magnetic interactions in TmIG. Achieving PMA with appropriate spin-wave damping can be crucial for novel device applications. It is worth noting that YbIG may serve as a viable alternative material to TmIG, EuIG, and other PMA garnets for studying spintronic and spin caloritronic phenomena due to its high spin-orbit coupling and comparable spin-wave damping [17,22]. YbIG has been explored in the single crystal or bulk form for its various properties [23–25], but there is no study yet reported for the same in the thin film form. This is despite the fact that it has the potential to be a promising material for spintronic and magnonic devices.

In this paper, we have comprehensively investigated structural, magnetic, and dynamical properties of YbIG films for different thicknesses. Moreover, our findings illustrate a general approach to tailor the PMA in REIG films by the controlled application of strain. We have been able to achieve PMA in YbIG thin film due to the strain-induced anisotropy. Results presented in this paper will be helpful for the development of novel spintronic and magnonic devices.

II. EXPERIMENTAL DETAILS

The thin films of YbIG on GGG(111) substrates were grown using pulsed laser deposition equipped with COMPex Pro 201, LAMBDA PHYSIK ($\lambda = 248$ nm) KrF excimer laser source. The target used for deposition was prepared using solid-state reaction with final heating at 1400 °C. To ensure the phase purity after final heating, the YbIG powder x-ray diffraction (XRD) data is fitted using FullProf software (Fig. 1). The space group Ia-3d was used to model the structure, and the refinement yielded a cubic structure with lattice parameters: $a = b = c = 12.302$ Å. All the films were grown at optimized deposition parameters. The laser energy was fixed

*zakir@iitk.ac.in

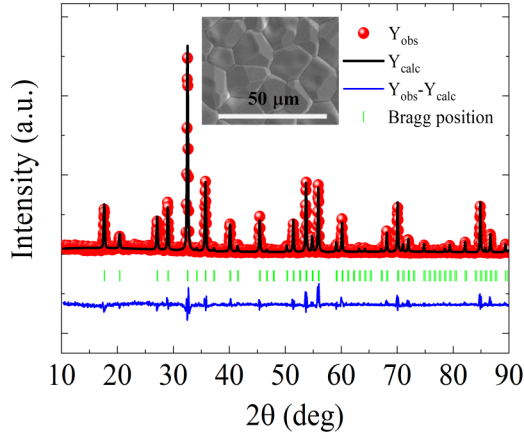


FIG. 1. Rietveld refined x-ray diffraction pattern for YbIG powder annealed at 1400 °C. Inset shows the SEM image of compact YbIG pellet annealed at 1400 °C.

at 200 mJ with a frequency of 2 Hz. The substrate temperature and chamber pressure were maintained at 750 °C and 4.0×10^{-2} mbar, respectively. Prior to deposition, the chamber was evacuated to a base pressure of 3.0×10^{-6} mbar. Films of different thickness were grown by varying the deposition time, while keeping all other parameters fixed. After deposition, the films were annealed *in situ* at the deposition temperature and pressure for 10 minutes. The samples were then cooled from growth temperature to 200 °C at a rate of 10 °C/min., and then allowed to cool naturally. The grown samples were characterized by XRD to determine their crystal structure and phase formation. Reciprocal space mapping (RSM) was performed to assess the epitaxial nature and strain state of the grown

films. Room-temperature (RT) magnetization measurements were performed using vibrating sample magnetometer (VSM) in a Quantum Design Physical Properties Measurement System (PPMS). We used the magneto-optical Kerr (MOKE) microscope of M/s Evico Magnetics, Germany, to perform RT MOKE measurements in longitudinal and polar geometries for the IP and out-of-plane (OOP) magnetization (\vec{M}) components. Ferromagnetic resonance (FMR) measurements were carried out using a custom-made broadband FMR spectrometer with a 300- μm wide coplanar waveguide (CPW). The FMR spectrometer was equipped with a microwave signal generator (ROHDE and SCHWARZ make SMB100A) of frequency range 1–20 GHz, lock-in amplifier, electromagnet, crystal diode detector, and an ac current source to drive the Helmholtz coil. The thin film is mounted on CPW by flip chip technique, which is housed in between pole gaps of electromagnet. The field modulation lock-in detection technique is used to record the first derivative of the FMR absorption spectra, where a DC magnetic field was swept at a fixed frequency.

III. RESULTS AND DISCUSSION

A. Structural analysis

In Fig. 2(a), XRD $2\theta - \omega$ scans for all the films are presented. The dotted line within the figure shows the position of YbIG thin film peak for different thicknesses, which is used to extract the OOP lattice parameter. The presence of Laue oscillations in Fig. 2(a) is indicative of their high crystalline quality and uniform thickness. The coinciding ϕ scan peaks for film and substrate along asymmetric (642) plane in Fig. 2(b) infers about the epitaxial growth of YbIG film on GGG substrate. Figure 2(c) presents the x-ray reflectivity data for films of

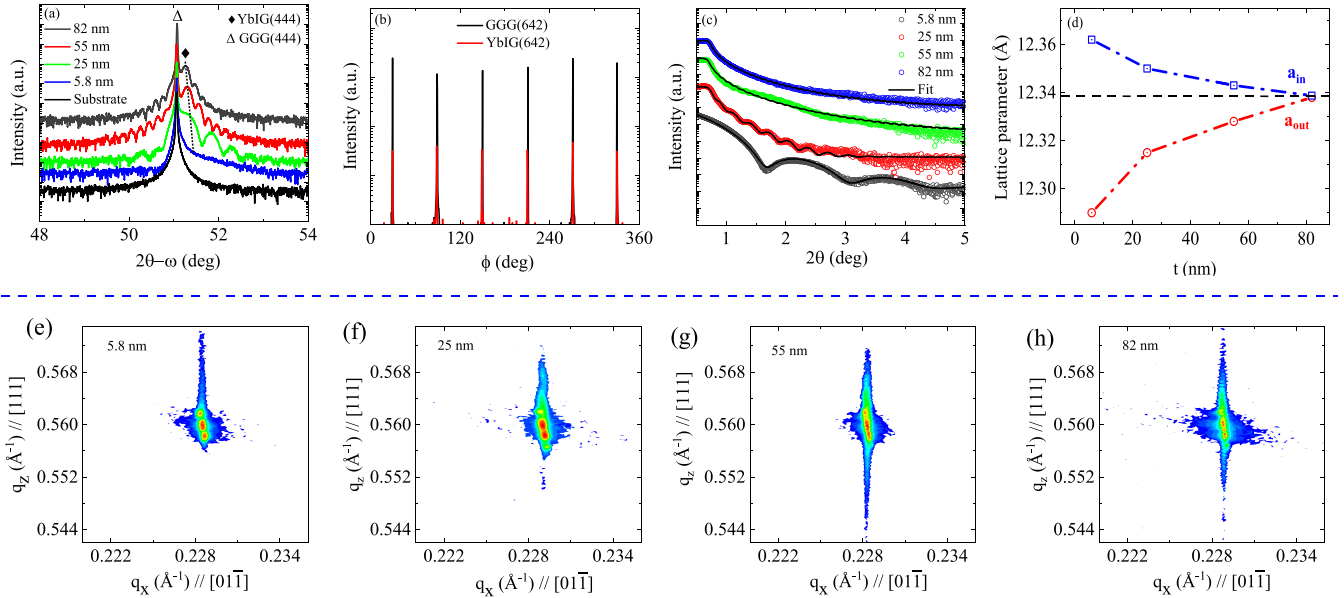


FIG. 2. (a) XRD $2\theta - \omega$ scans for different grown thicknesses of YbIG films and for the GGG substrate. (b) ϕ scans along 642 plane for 25-nm-thick YbIG film and for the GGG substrate. (c) X-ray reflectivity (XRR) for epitaxial YbIG films grown on top of the GGG(111) substrates, (d) plot of lattice parameter “ a_{in} and a_{out} ” vs thickness (t) variation of YbIG films. (e)–(h) Reciprocal space maps (RSM) along asymmetric (642) plane for different thicknesses of the YbIG/GGG(111) films.

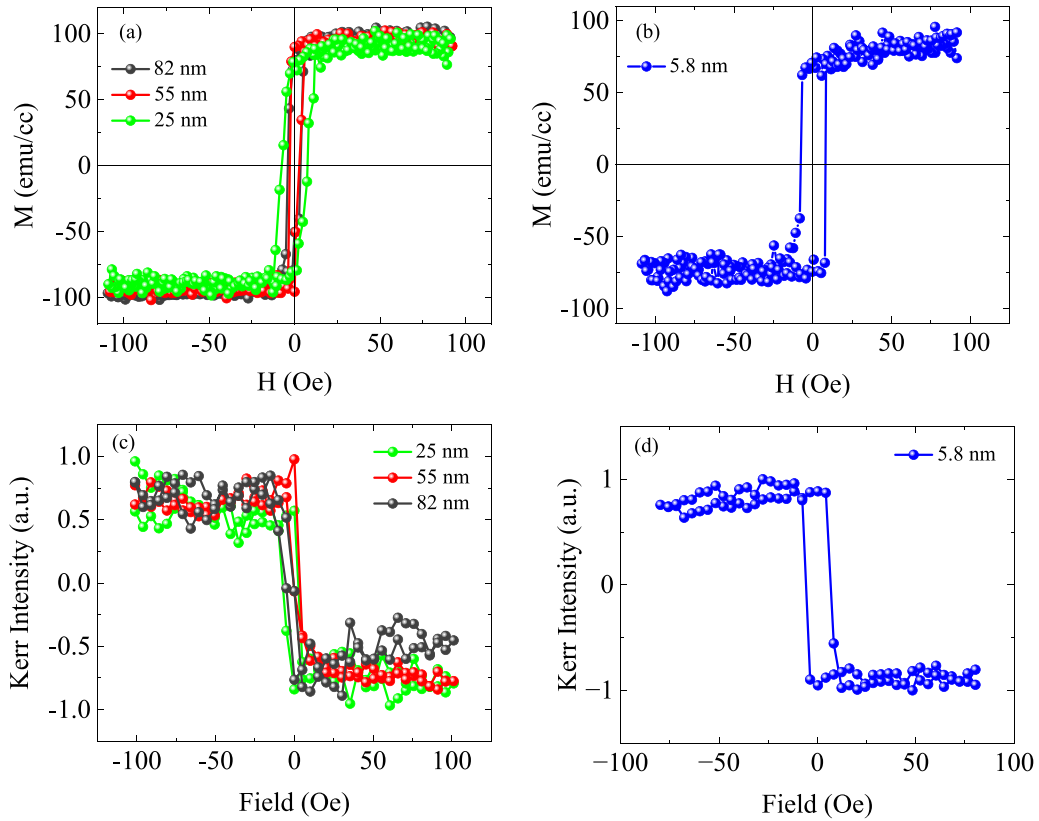


FIG. 3. M-H loops of YbIG/GGG(111) thin films measured for (a) in-plane (IP) and (b) out-of-plane (OOP) configuration at room temperature. (c) MOKE hysteresis loops for longitudinal and (d) polar geometry.

the indicated thickness. We performed a fitting analysis using the X'pert Pro reflectivity software to determine the thickness and roughness of the films. The surface and interface roughness is found to be <0.8 nm for all the thicknesses of YbIG/GGG(111) thin films. The observed variation in the OOP lattice parameter [Fig. 2(d)] with film thickness suggests the presence of IP tensile strain. This observation is consistent with expectations, given that the bulk lattice parameter of YbIG is smaller than that of the GGG substrate. Notably, the YbIG peak in Fig. 2(a) shift gradually towards lower 2θ values with increasing YbIG film thickness, indicating an increase in the OOP lattice parameter (a_{out}). This suggests that strain in the film is getting relaxed with increasing thickness, possibly through creation of interfacial distortions. The observed value of strain ranges from ~ 0 to -0.40% as the thickness of YbIG film decreases. To further investigate the strain state of the films, we conducted RSM for asymmetric (642) crystallographic planes. Asymmetric RSM scans allow us to probe the strain state of the YbIG films along the $[01\bar{1}]$ IP direction. Figures 2(e)–2(h) display the RSM data around the (642) plane for all the films, revealing a coherent lattice match between the film and the substrate in the IP direction. The lattice parameters have been calculated for the grown YbIG films using the formula for the IP lattice parameter, $a_{\text{in}} = (2\sqrt{2})/q_x$, and for the OOP lattice parameter, $a_{\text{out}} = (4\sqrt{3})/q_z$. The parameters a_{in} and a_{out} are plotted as a function of thickness (t) in Fig. 2(d).

B. Magnetization and MOKE analysis

To investigate the magnetization behavior of YbIG thin films and the influence of film thickness on IP and OOP magnetization, we conducted RT VSM measurements using a Quantum Design PPMS system. Figure 3(a) illustrates IP hysteresis loops for 25, 55, and 82-nm-thick films whereas Fig. 3(b) shows OOP hysteresis for 5.8-nm-thick film. The linear paramagnetic contribution arising from substrate was subtracted from the raw data of magnetization hysteresis loops. We have not shown the hard-axis loops in the figure due to significant error associated with subtracting the paramagnetic contribution from the substrate, especially at higher magnetic fields needed for hard-axis magnetization saturation. The coercivity H_c values are found in the range 2–8 Oe, and the calculated saturation magnetization values using M-H loops are listed in Table I. Furthermore, we have also conducted MOKE measurements at room temperature in both longitudinal (L-MOKE) and perpendicular (P-MOKE) geometries. Notably, the MOKE data reveals square-like hysteresis in the P-MOKE geometry for the thickness of 5.8 nm [Fig. 3(d)], whereas for higher thicknesses, square hysteresis loops are observed in the L-MOKE geometry [Fig. 3(c)]. Therefore, the data obtained from both VSM and MOKE measurements unambiguously indicate a transition from an IP to an OOP easy-axis magnetization as the film thickness decreases. This transition of easy-axis magnetization can primarily be attributed to the epitaxial strain induced anisotropy, which is enhanced with decreasing film thickness. To gain

TABLE I. The list of various parameters extracted from numerical fitting of FMR measurements for YbIG films with thickness variation. K_{shape} is calculated using the M_s value from magnetization data, while K_o is calculated using the XRD data.

t (nm)	$4\pi M_s$ (Oe)	K_σ ($\times 10^4$ erg/cc)	K_{shape} ($\times 10^4$ erg/cc)	K_1 ($\times 10^3$ erg/cc)	K_2 ($\times 10^3$ erg/cc)	K_\perp ($\times 10^4$ erg/cc)	K_{eff} ($\times 10^4$ erg/cc)	H_A Oe	H_{eff} Oe	α ($\times 10^{-2}$)
82	1206	-0.04	5.78	-1.2	1.50	0.04	5.8	18	1188	3.501
55	1005	-0.92	4.01	-1.1	2.80	0.5	3.3	130	877	2.775
25	980	-2.1	3.82	-0.8	3.10	1.8	2.0	460	517	3.181
5.8	816	-4.2	2.65	-0.64	3.30	3.7	-1.3	1100	-309	3.346

further insights into the contributions of different magnetic anisotropy factors in achieving PMA, FMR measurements were conducted, which is discussed in the following section.

C. FMR analysis

The FMR technique provides a pathway to explore all the magnetic coefficients that define the energy density of a magnetic thin film. The frequency and angular (IP and OOP) variation of FMR spectra allow to determine key parameters such as the gyromagnetic ratio, effective magnetization, magnetic anisotropy, and damping constant very precisely. Figure 4(a) shows a schematic illustration of the polar coordinate system to represent the direction of magnetization, applied magnetic field, and anisotropy in our (111) oriented epitaxial YbIG films. The IP angle between the \vec{H} (\vec{M}) and the $[2\bar{1}\bar{1}]$ direction is denoted by φ_H (φ_M). The polar angle between \vec{H} (\vec{M}) and the $[111]$ direction is denoted by θ_H (θ_M).

The free energy density that characterizes the magnetization of a ferrimagnetic film with a cubic structure can be expressed as follows [26,27]:

$$F = -\vec{H} \cdot \vec{M} + 2\pi(\vec{M} \cdot \hat{e}_z)^2 - \frac{K_\perp}{M^2}(\vec{M} \cdot \hat{e}_z)^2 + K_1(M_x^2 M_y^2 + M_y^2 M_z^2 + M_z^2 M_x^2) + K_2 M_x^2 M_y^2 M_z^2. \quad (1)$$

The first term stands for the Zeeman energy, second term for dipolar demagnetization energy, third term for uniaxial perpendicular magnetic anisotropy energy. The last two terms stand for the first and second-order cubic magnetocrystalline anisotropy (MCA) energies. The MCA energy expression for $[111]$ oriented cubic crystal can be deduced using the polar coordinate system, as depicted in Fig. 4(a), based on the

magnetization direction cosines with respect to the primary cubic axes.

The direction cosines are represented as

$$\begin{aligned} M_x &= \frac{1}{\sqrt{3}} \cos \theta_M + \frac{2}{\sqrt{6}} \sin \theta_M \cos \varphi_M, \\ M_y &= \frac{1}{\sqrt{3}} \cos \theta_M - \frac{1}{\sqrt{6}} \sin \theta_M \cos \varphi_M + \frac{1}{\sqrt{2}} \sin \theta_M \sin \varphi_M, \\ M_z &= \frac{1}{\sqrt{3}} \cos \theta_M - \frac{1}{\sqrt{6}} \sin \theta_M \cos \varphi_M - \frac{1}{\sqrt{2}} \sin \theta_M \sin \varphi_M. \end{aligned} \quad (2)$$

The explicit form of Eq. (1) can be expressed as follows:

$$\begin{aligned} F &= -M_s H \left[\begin{aligned} &\sin \theta_H \sin \theta_M \cos(\varphi_H - \varphi_M) \\ &+ \cos \theta_H \cos \theta_M \end{aligned} \right] \\ &+ 2\pi M_s^2 \cos^2 \theta_M - K_\perp \cos^2 \theta_M \\ &+ \frac{K_1}{12} (7 \sin^4 \theta_M - 8 \sin^2 \theta_M + 4 \\ &- 4\sqrt{2} \sin^3 \theta_M \cos \theta_M \cos 3\varphi_M) \\ &+ \frac{K_2}{108} (-24 \sin^6 \theta_M + 45 \sin^4 \theta_M - 24 \sin^2 \theta_M \\ &+ 4 - 2\sqrt{2} \sin^3 \theta_M \cos \theta_M (5 \sin^2 \theta_M - 2) \cos 3\varphi_M \\ &+ \sin^6 \theta_M \cos 6\varphi_M). \end{aligned} \quad (3)$$

The coefficients K_\perp , K_1 , and K_2 are denoted as the uniaxial perpendicular magnetic anisotropy constant, first- and second-order cubic MCA constants, respectively. The resonance frequency f_r of the uniform \vec{M} precession given by

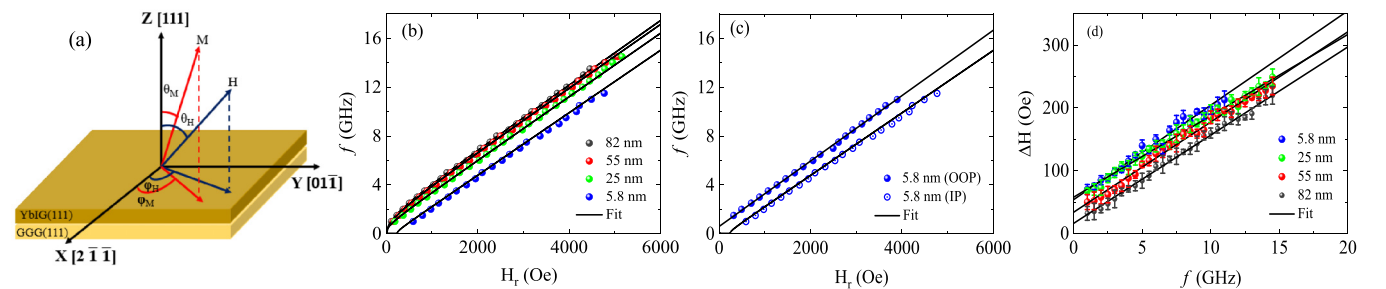


FIG. 4. (a) Schematic of FMR measurement configurations, \vec{H} and \vec{M} represent the direction of applied magnetic field and magnetization. (b) In-plane frequency variation of resonance field H_r . (c) In-plane and out-of-plane frequency variation of resonance field H_r for the lowest thickness with PMA. (d) In-plane frequency variation of FMR linewidth ΔH . The solid spherical dots are the experimental data points while black solid lines represent fit to the experimental data.

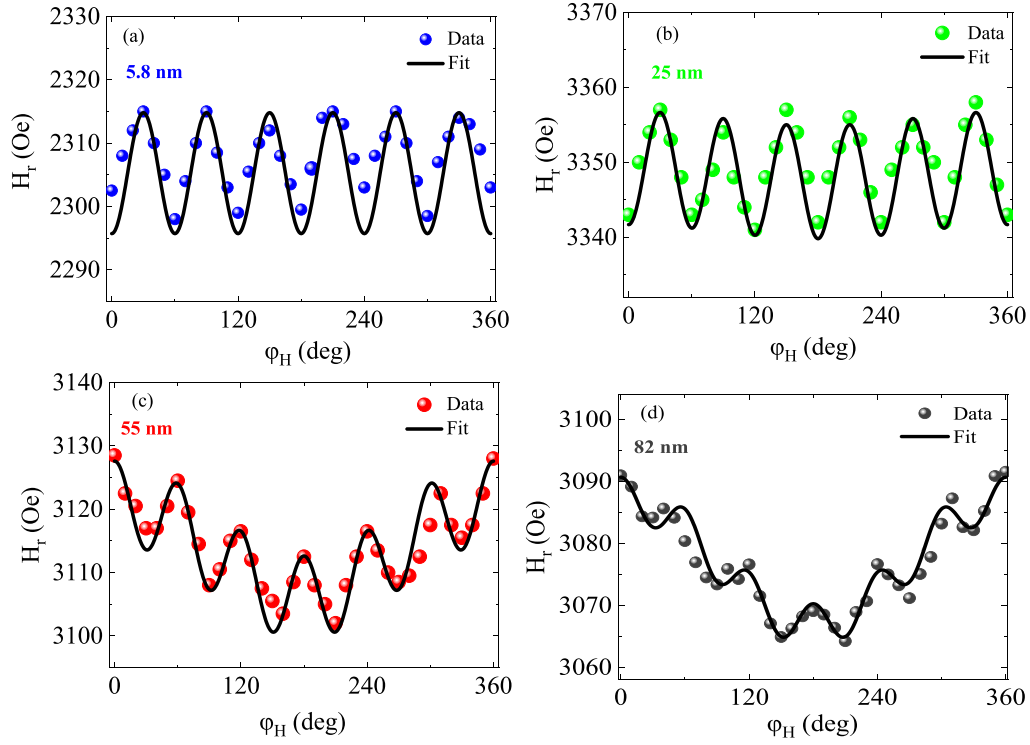


FIG. 5. FMR azimuthal angle φ_H variation of H_r . The data were acquired at a frequency of 5.5 GHz for YBIG film with lowest thickness of 5.8 nm and at 9.5 GHz for higher thicknesses. Solid spherical dots represents the experimental data points while black solid line represents the model fit.

Smit and Beljers [28],

$$f_r^2 = \left(\frac{\gamma}{2\pi} \right)^2 \frac{1}{M_S^2 \sin^2 \theta_M} \left[\frac{\partial^2 F}{\partial \varphi_M^2} \frac{\partial^2 F}{\partial \theta_M^2} - \left(\frac{\partial^2 F}{\partial \theta_M \partial \varphi_M} \right)^2 \right]. \quad (4)$$

Here, $\gamma = \frac{g\mu_B}{\hbar}$, where g denotes the Landé g factor, and μ_B is the Bohr magneton. The equilibrium angles of magnetization, φ_M and θ_M , were determined numerically by solving the coupled and indirectly defined functional equations after energy minimization ($\frac{\partial F}{\partial \varphi_M} = \frac{\partial F}{\partial \theta_M} = 0$) using *Mathematica*. The values of φ_M and θ_M obtained for respective values of φ_H and θ_H were utilized to model the angular variations of resonance field (H_r vs φ_H and H_r vs θ_H).

We performed IP (φ_H) and OOP (θ_H) angular variations at frequencies 9.5 GHz for the higher thicknesses, and at 5.5 GHz for lowest thickness. The φ_H rotation is performed intentionally from the $[2\bar{1}\bar{1}]$ direction to simplify the experimental procedure and the numerical model fitting. The φ_H variation of H_r as shown in Fig. 5 unveil a subtle IP magnetic anisotropy with a pronounced distinct sixfold symmetry. This cordially matches the crystal symmetry of YBIG. We simulate the H_r vs φ_H from the numerical model fitting using Eqs. (3) and (4). The K_2 term in Eq. (3) with sixfold symmetry plays a significant role to fit the experimental data for the lower thickness films of 5.8 and 25 nm. A weak unidirectional feature in magnetic anisotropy is observed in higher thickness films of 56 and 85 nm. For higher thicknesses, we introduced an additional exchange anisotropy (K_{EA}) term, $-K_{EA} \sin \theta_M \cos \varphi_M$, to the total free energy density in Eq. (3) to fit the unidirectional feature. The experimental data yielded a good fit and

the values of anisotropies are listed in Table I. We recorded FMR spectra over a frequency spectrum along the IP easy- and hard-axis for each film. However, the IP anisotropy of 10–30 Oe did not cause any substantial variation in trends of frequency variation of H_r . The H_r vs f along the IP easy-axis for all the thicknesses is displayed in Fig. 4(b). The presence of various anisotropies and interactions leads to the precession of magnetic moments within an effective magnetic field H_{eff} , differs from the externally applied field H . This effective field can be estimated directly using Kittel's equation [29]. Kittel's equation has been used to fit the f vs H_r at resonance condition and can be written as $f = (\gamma/2\pi)[H_r(H_r + 4\pi M_{\text{eff}})]^{1/2}$ for $\theta_H = 90^\circ$ and $f = (\gamma/2\pi)(H_r - 4\pi M_{\text{eff}})$ for $\theta_H = 0^\circ$. The curve fitting gives the values of γ and effective magnetization ($4\pi M_{\text{eff}}$), listed in Table I. The $4\pi M_{\text{eff}}$ has a relation with saturation magnetization (M_S) and the effective anisotropy field (H_A): $4\pi M_{\text{eff}} = 4\pi M_S - H_A$, where $H_A = \frac{2K_1}{M_S} - \frac{4K_1}{3M_S} - \frac{4K_2}{9M_S}$ is the total anisotropy field along the $[111]$ direction. The $4\pi M_{\text{eff}}$ values exhibit a decline with decreasing thickness, eventually becoming negative for the lowest thickness. The negative value of $4\pi M_{\text{eff}}$ indicates the IP to OOP switching of the magnetic easy-axis. In Fig. 4(c), we also performed frequency variation in OOP orientation for the 5.8-nm-thick film, as it depicts OOP magnetic easy-axis. The OOP angular variation of H_r gives direct evidence of PMA in the magnetic thin films, and the plots are displayed in Fig. 6. The higher thicknesses shows magnetic easy-axis lies along the film plane with H_r minima at $\theta_H = 90^\circ$, while the lowest thickness shows magnetic easy-axis along direction perpendicular to film plane with H_r minima at $\theta_H = 0^\circ$. The

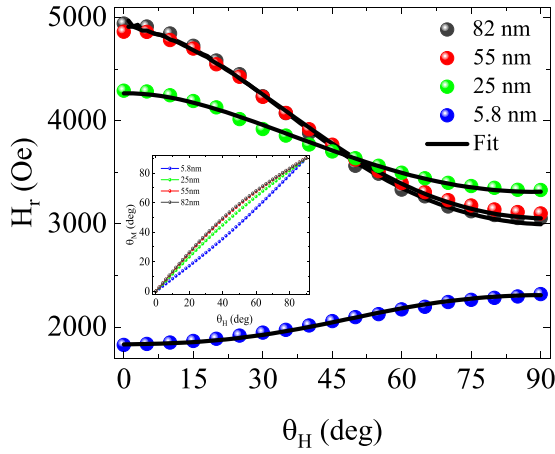


FIG. 6. FMR Polar angle θ_H variation of H_r . The data were recorded at a frequency of 5.5 GHz for 5.8-nm-thick YbIG film and at 9.5 GHz for higher thicknesses. Solid spherical dots represents the measured data points while black solid line represents the model fit. Inset shows the θ_M vs θ_H plots for all the films.

OOP angular variation shows a trend of transition from IP to OOP for magnetic easy-axis with decreasing film thickness. This trend is also observed for the magnetization and MOKE data in Fig. 3. The reorientation of easy-axis from IP to OOP is a result of the PMA field exerting a dominant influence over the demagnetization field. The numerical model fitting to the experimental data yielded the parameters listed in Table I. The K_{\perp} values for lower film thickness are found to be large with positive magnitude of the order of $\sim 10^4$ erg/cc.

The effective magnetic anisotropy K_{eff} can be written as the sum of the various contributions [30],

$$K_{\text{eff}} = K_{\text{crystal}[111]} + K_{\text{shape}} + K_{\sigma} + K_{\text{Growth}}. \quad (5)$$

$K_{\text{crystal}[111]}$ comprises K_1 and K_2 , and has been found to have the lowest contributions to the total anisotropy. These are intrinsic anisotropies and originate as a result of interplay between crystal symmetry, electronic structure, and atomic interactions, i.e., spin-orbit interactions [31]. K_{shape} represents the shape anisotropy arises from the geometry of the crystal. It is calculated by using the formula $K_{\text{shape}} = 2\pi M_S^2$, where M_S is saturation magnetization of the sample. The shape anisotropy has a demagnetization effect on the total anisotropy, which favors the IP orientation of \vec{M} . The magnetoelastic anisotropy (MEA) originate as a result of epitaxial strain in the system due to lattice mismatch between the film and the substrate. The MEA is calculated as $K_{\sigma} = -\frac{3}{2}\lambda_{111}\sigma_{\parallel}$, where σ_{\parallel} is the IP induced strain, depend on the relative mismatch between the lattice parameters of the substrate (a_{bulk}) and film (a_{film}) along [111] direction, $\sigma_{\parallel} = \frac{E}{1+\nu} \frac{a_{\text{film}} - a_{\text{bulk}}}{a_{\text{bulk}}}$. Here E and ν denotes Young's modulus and Poisson ratio, respectively. For our calculations, we adopted the reported values $E = 200$ GPa and $\nu = 0.29$ for $\text{Y}_3\text{Fe}_5\text{O}_{12}$ [32]. It is worth noting that, for YbIG, these material constants have not yet been reported in literature. K_{Growth} represents the growth-induced anisotropy, which may arise during the growth of iron garnet thin films with two or more rare-earth ions of distinct sizes. The kinetics of preferential rare-earth cation incorporation at dodecahedral sites lead to crystal symmetry breaking which

generates another uniaxial anisotropy in the system, known as growth-induced anisotropy. K_{Growth} is excluded here, as Yb^{3+} is the only rare-earth ion in the YbIG system [33,34]. MCA and MEA together tries to overcome the shape anisotropy, and make the magnetic easy-axis perpendicular or away from the film plane.

The magnetic damping is a very important parameter for the understanding of the dynamical behavior of magnetic materials and their stability for various device applications. The FMR linewidth is a measure of magnetic damping, which is associated with the magnetic relaxation process and, consequently, energy dissipation in the system. Gilbert- and non-Gilbert-type relaxation are the two main mechanisms that contribute to the damping in the system. Gilbert type is most common and intrinsic relaxation, occurs due to interaction between magnetization and the lattice. Non-Gilbert-type relaxation occurs due to defects, impurities or inhomogeneity in the system, and is generally weaker than Gilbert-type relaxation. Landau-Lifshitz-Gilbert equation estimates the damping by the expression [35,36]

$$\Delta H = \Delta H_0 + \frac{2}{\sqrt{3}} \frac{2\pi\alpha}{\gamma} f. \quad (6)$$

ΔH_0 represents the magnetic inhomogeneity in the system, while the second term represents the intrinsic Gilbert damping. The fitting of linewidth data in Fig. 4(d) using Eq. (6) directly yields the values of α and ΔH_0 . The values of α for the respective thicknesses are listed in Table I. The α values are of the order of 10^{-2} , which is comparable to the most explored garnet (TmIG $\sim 10^{-2}$) with PMA [8,37]. The comparable damping parameter and higher spin-orbit coupling in YbIG [38] hold significant promise for advancing research on spin-related phenomena and facilitating potential applications in spintronic devices.

The ever-growing field of spintronics and magnonics continuously seeks new iron garnet thin films that can manifest diverse magnetization behaviors, anisotropies, compensation points, spin-wave damping characteristics, and a host of other distinctive properties. For the same purpose, we have grown YbIG thin films on the GGG(111) substrates, which are not yet explored to best of our knowledge. YbIG on top of GGG(111) experiences tensile strain due to lattice mismatch between film and substrate. YbIG possess negative value of magnetostriction coefficient, $\lambda_{111} = -4.5 \times 10^{-6}$ [39]. It is well established that PMA in garnet thin films can be achieved with clever balancing of magnetostriction (λ) and elastic strain. There are reports in literature that IP tensile strain with negative magnetostriction [40–42] and IP compressive strain with positive magnetostriction [17,43] produces PMA in the garnets. Fu *et al.* [30] explored PMA in nm-thick YIG films. The relaxation of strain before inducing a sufficiently large anisotropy leads to IP magnetic anisotropy in YIG. They employed $\text{Sm}_3\text{Fe}_5\text{O}_{12}$ layer as a buffer to alleviate the relaxation of the strain at the interface. The PMA in another YIG has been explored by growing the nm-thick films on top of $\text{Gd}_3\text{Sc}_2\text{Ga}_3\text{O}_{12}$ (GSGG) substrates, which has larger lattice mismatch producing sustainable IP tensile strain. The IP tensile strain in combination with negative λ produces PMA. They reported PMA field $H_{\perp} = 2800$ Oe and $\alpha \sim 10^{-3}$ – 10^{-4} [14]. PMA in a material along different

orientation of GGG substrate has been explored in EuIG for (001) and (111) orientations with α in the order of $\sim 10^{-2}$ [17]. For TmIG, there are several reports on realization of strong PMA due to strain-induced MEA with tensile strain and damping in order of $\sim 10^{-2}$. There is a report on strong tuning of H_{\perp} and tensile strain with increasing Fe concentration for TmIG [8]. In another report, they revealed robust PMA in sub-10-nm TmIG/GGG(111) with saturation magnetization close to bulk reported for TmIG [41]. Ortiz *et al.* [43] showed the general approach for tuning magnetic anisotropy using modulation of strain with epitaxial growth.

We observed PMA in YbIG thin film for sub-10-nm thickness (5.8 nm) and a trend of transition from IP to OOP with the decreasing thickness. This is because, as the thickness decreases, strain state of YbIG/GGG(111) changes, can be seen clearly in Figs. 2(e)–2(h). The induced strain results in enhanced MEA. The MEA along with MCA compete with shape anisotropy, and at a certain value of strain, it overcomes the shape anisotropy and produces PMA in the system. For PMA to occur, the required condition is $|K_{\text{crystal}} + K_{\sigma}| > |K_{\text{shape}}|$; which leads to a negative value of effective anisotropy ($K_{\text{eff}} < 0$). The lowest thickness of YbIG film exhibits $K_{\text{eff}} < 0$, which confirms the PMA. The M_s value of YbIG films increases with increasing thickness due to improved crystallinity, which is confirmed by the presence of Laue oscillations. Notably, the lowest thickness (5.8 nm) displays strain-induced anisotropy $K_{\sigma} = -4.2 \times 10^4$ erg/cc, which exceeds the shape anisotropy $K_{\text{shape}} = 2.65 \times 10^4$ erg/cc. This is a strong proof that strain can induce large enough PMA to overcome shape anisotropy of a thin film. Moreover, the α value for YbIG is comparable to other PMA garnets EuIG [44] and TmIG [8]. Although there is a possibility of Gd and/or Ga interdiffusion at the film/substrate interface, which can influence the properties of the REIG thin films [45–47]. The thickness of the interdiffusion layer may vary from 0 to even 6 nm depending on the growth conditions of the film, mostly affected by high-temperature growth or annealing processes. Such an interdiffusion layer, for example, the formation of Gd-doped YIG in the case of YIG film growth on GGG, may affect the low-temperature evolution of magnetization [45] and Gilbert damping in FMR measurements [47]. Additionally, there may be inversion symmetry breaking at the interface diffusion, leading to interfacial Dzyaloshinskii-Moriya interaction (iDMI) responsible for the formation of chiral domain walls and skyrmion spin textures [46]. In our YbIG films on GGG, a dead layer approximately 1.2-nm thick was detected at the interface by analyzing the thickness variation of magnetization per unit area. However, no specific impact of interdiffusion on magnetization and damping parameter α was observed for the 5.8-nm-thick YbIG film.

The quest for iron garnet with a low value of α and PMA has been a long standing goal for researchers since the past decade. For the matter of fact that there has been a lot of studies on TmIG and other PMA garnets for harnessing various properties and phenomena. In this context, our results on YbIG with PMA and moderate α has strong potential in the field of spintronics and magnonics. Researchers may find thin films of YbIG with PMA particularly intriguing for the following potential research perspective: (1) YbIG can prove itself an alternative of PMA iron garnets. (2) Tuning the film composition results in sustainable strain, and hence PMA in thicker YbIG films can be achieved with better parameters. (3) Optimization of growth process can lead to PMA with better α , and that can be crucial for spin-transport studies and for manipulation of domain wall motion via spin-orbit torque effects.

IV. CONCLUSIONS

To summarize, we have successfully deposited high quality epitaxial YbIG films on GGG(111) substrates, a critical step towards utilizing YbIG thin films in spintronic and magnonic devices. FMR IP angular variation shows sixfold symmetry, which emphasizes the significant contribution from second-order magnetocrystalline anisotropy. The M-H and MOKE data infers about OOP easy-axis for lowest thickness (5.8 nm) of YbIG film, which is further confirmed with FMR measurements. Polar angle variation in FMR shows transition from IP to OOP magnetization easy-axis with thickness variation, and shows PMA for the lowest thickness. The K_{\perp} values for lowest thicknesses are found to be large, with positive value of the order of $\sim 10^4$ erg/cc, which leads to switching of \vec{M} towards out-of-plane. The finding of PMA in sub-10-nm-thick film is significant for memory device applications. The damping factor $\alpha \sim 10^{-2}$ is comparable to that of TmIG and EuIG, which are the most explored PMA garnets for novel spin-transport phenomena. The damping factor is an important parameter that influences device performance in terms of speed, stability, energy efficiency, and signal quality. The PMA in YbIG with moderate α can be a promising alternative to TmIG and EuIG. The results present in this paper are expected to stimulate further research in the context of its viability as a promising materials for spintronics and magnonics applications.

ACKNOWLEDGMENTS

We gratefully acknowledge the research support from IIT Kanpur and DST, Government of India [Sanction Order No. DST/NM/TUE/QM-06/2019(G)], and SERB, Government of India [Sanction Order No. CRG/2022/002665]. The authors would like to thank UGC-DAE-CSR, Indore, for providing access to PLD facility.

- [1] S.-Z. Lin, C. D. Batista, C. Reichhardt, and A. Saxena, Ac current generation in chiral magnetic insulators and skyrmion motion induced by the spin Seebeck effect, *Phys. Rev. Lett.* **112**, 187203 (2014).
 [2] X.-P. Zhang, F. S. Bergeret, and V. N. Golovach, Theory of spin Hall magnetoresistance from a microscopic perspective, *Nano Lett.* **19**, 6330 (2019).

- [3] M. Matsuo, Y. Ohnuma, T. Kato, and S. Maekawa, Spin current noise of the spin Seebeck effect and spin pumping, *Phys. Rev. Lett.* **120**, 037201 (2018).
 [4] Z. Wang, C. Tang, R. Sachs, Y. Barlas, and J. Shi, Proximity-induced ferromagnetism in graphene revealed by the anomalous Hall effect, *Phys. Rev. Lett.* **114**, 016603 (2015).

- [5] B. Miao, S. Y. Huang, D. Qu, and C. L. Chien, Inverse spin Hall effect in a ferromagnetic metal, *Phys. Rev. Lett.* **111**, 066602 (2013).
- [6] C. Hauser, T. Richter, N. Homonnay, C. Eischschmidt, M. Qaid, H. Deniz, D. Hesse, M. Sawicki, S. G. Ebbinghaus, and G. Schmidt, Yttrium iron garnet thin films with very low damping obtained by recrystallization of amorphous material, *Sci. Rep.* **6**, 20827 (2016).
- [7] H. Chang, P. Li, W. Zhang, T. Liu, A. Hoffmann, L. Deng, and M. Wu, Nanometer-thick yttrium iron garnet films with extremely low damping, *IEEE Magn. Lett.* **5**, 1 (2014).
- [8] C. N. Wu, C. C. Tseng, Y. T. Fanchiang, C. K. Cheng, K. Y. Lin, S. L. Yeh, S. R. Yang, C. T. Wu, T. Liu, M. Wu, M. Hong, and J. Kwo, High-quality thulium iron garnet films with tunable perpendicular magnetic anisotropy by *off-axis* sputtering—Correlation between magnetic properties and film strain, *Sci. Rep.* **8**, 11087 (2018).
- [9] S. Vélez, J. Schaab, M. S. Wörnle, M. Müller, E. Gradauskaitė, P. Welter, C. Gutzwiller, C. Nistor, C. L. Degen, M. Trassin *et al.*, High-speed domain wall racetracks in a magnetic insulator, *Nat. Commun.* **10**, 4750 (2019).
- [10] J. J. Bauer, E. R. Rosenberg, S. Kundu, K. A. Mkhoyan, P. Quarterman, A. J. Grutter, B. J. Kirby, J. A. Borchers, and C. A. Ross, Dysprosium iron garnet thin films with perpendicular magnetic anisotropy on silicon, *Adv. Electron. Mater.* **6**, 1900820 (2020).
- [11] K. Lal, R. Kumar, P. Ghising, B. Samantary, and Z. Hossain, Oblique magnetic anisotropy and domain texture in $\text{Bi}_3\text{Fe}_5\text{O}_{12}$ films, *Phys. Rev. B* **108**, 014401 (2023).
- [12] M. X. Guo, C. K. Cheng, Y. C. Liu, C. N. Wu, W. N. Chen, T. Y. Chen, C. T. Wu, C. H. Hsu, S. Q. Zhou, C. F. Chang *et al.*, Single-crystal epitaxial europium iron garnet films with strain-induced perpendicular magnetic anisotropy: structural, strain, magnetic, and spin transport properties, *Phys. Rev. Mater.* **6**, 054412 (2022).
- [13] H. Yamahara, M. Mikami, M. Seki, and H. Tabata, Epitaxial strain-induced magnetic anisotropy in $\text{Sm}_3\text{Fe}_5\text{O}_{12}$ thin films grown by pulsed laser deposition, *J. Magn. Magn. Mater.* **323**, 3143 (2011).
- [14] J. Ding, C. Liu, Y. Zhang, U. Erugu, Z. Quan, R. Yu, E. McCollum, S. Mo, S. Yang, H. Ding, X. Xu, J. Tang, X. Yang, and M. Wu, Nanometer-thick yttrium iron garnet films with perpendicular anisotropy and low damping, *Phys. Rev. Appl.* **14**, 014017 (2020).
- [15] S. Ding, Z. Liang, C. Yun, R. Wu, M. Xue, Z. Lin, A. Ross, S. Becker, W. Yang, X. Ma *et al.*, Anomalous Hall effect in magnetic insulator heterostructures: Contributions from spin-Hall and magnetic-proximity effects, *Phys. Rev. B* **104**, 224410 (2021).
- [16] C. O. Avci, A. Quindeau, C.-F. Pai, M. Mann, L. Caretta, A. S. Tang, M. C. Onbasli, C. A. Ross, and G. S. D. Beach, Current-induced switching in a magnetic insulator, *Nat. Mater.* **16**, 309 (2017).
- [17] E. R. Rosenberg, L. Beran, C. O. Avci, C. Zeledon, B. Song, C. Gonzalez-Fuentes, J. Mendil, P. Gambardella, M. Veis, C. Garcia *et al.*, Magnetism and spin transport in rare-earth-rich epitaxial terbium and europium iron garnet films, *Phys. Rev. Mater.* **2**, 094405 (2018).
- [18] C. O. Avci, E. Rosenberg, L. Caretta, F. Büttner, M. Mann, C. Marcus, D. Bono, C. A. Ross, and G. S. Beach, Interface-driven chiral magnetism and current-driven domain walls in insulating magnetic garnets, *Nat. Nanotechnol.* **14**, 561 (2019).
- [19] Q. Shao, Y. Liu, G. Yu, S. K. Kim, X. Che, C. Tang, Q. L. He, Y. Tserkovnyak, J. Shi, and K. L. Wang, Topological Hall effect at above room temperature in heterostructures composed of a magnetic insulator and a heavy metal, *Nat. Electron.* **2**, 182 (2019).
- [20] A. J. Lee, A. S. Ahmed, B. A. McCullian, S. Guo, M. Zhu, S. Yu, P. M. Woodward, J. Hwang, P. C. Hammel, and F. Yang, Interfacial Rashba-effect-induced anisotropy in nonmagnetic-material–ferrimagnetic-insulator bilayers, *Phys. Rev. Lett.* **124**, 257202 (2020).
- [21] S. Mokarian Zanjani and M. C. Onbaşlı, Predicting new iron garnet thin films with perpendicular magnetic anisotropy, *J. Magn. Magn. Mater.* **499**, 166108 (2020).
- [22] A. Chanda, C. Holzmann, N. Schulz, A. Ullrich, D. DeTellem, M. Albrecht, M. Gross, C. A. Ross, D. A. Arena, M.-H. Phan *et al.*, Temperature evolution of magnon propagation length in $\text{Tm}_3\text{Fe}_5\text{O}_{12}$ thin films: Roles of magnetic anisotropy and Gilbert damping, *ACS Nano* **18**, 7223 (2024).
- [23] K. A. Wickersheim and R. L. White, Anisotropy of exchange in ytterbium iron garnet, *Phys. Rev. Lett.* **8**, 483 (1962).
- [24] H. Watanabe and B. Brockhouse, Exchange field splitting in ytterbium iron garnet, *Phys. Rev.* **128**, 67 (1962).
- [25] S. Geller, J. Remeika, R. Sherwood, H. Williams, and G. Espinosa, Magnetic study of the heavier rare-earth iron garnets, *Phys. Rev.* **137**, A1034 (1965).
- [26] L. D. Landau and E. M. Lifshitz, *Electrodynamics of Continuous Media*, 2nd ed. (Pergamon Press, Oxford, 1984).
- [27] S. Lee, S. Grudichak, J. Sklenar, C. C. Tsai, M. Jang, Q. Yang, H. Zhang, and J. B. Ketterson, Ferromagnetic resonance of a YIG film in the low frequency regime, *J. Appl. Phys.* **120**, 033905 (2016).
- [28] J. Smit and H. G. Beljers, Ferromagnetic resonance absorption in $\text{BaFe}_{12}\text{O}_{19}$, a highly anisotropic crystal, *Philips Res. Rep.* **10**, 113 (1955).
- [29] E. Popova, A. F. F. Galeano, M. Deb, B. Warot-Fonrose, H. Kachkachi, F. Gendron, F. Ott, B. Berini, and N. Keller, Magnetic anisotropies in ultrathin bismuth iron garnet films, *J. Magn. Magn. Mater.* **335**, 139 (2013).
- [30] J. Fu, M. Hua, X. Wen, M. Xue, S. Ding, M. Wang, P. Yu, S. Liu, J. Han, C. Wang, H. Du, Y. Yang, and J. Yang, Epitaxial growth of $\text{Y}_3\text{Fe}_5\text{O}_{12}$ thin films with perpendicular magnetic anisotropy, *Appl. Phys. Lett.* **110**, 202403 (2017).
- [31] P. Gruszecki, C. Banerjee, M. Mruczkiewicz, O. Hellwig, A. Barman, and M. Krawczyk, Chapter Two - The influence of the internal domain wall structure on spin wave band structure in periodic magnetic stripe domain patterns, *Solid State Phys.* **70**, 79 (2019).
- [32] N. S. Sokolov, V. V. Fedorov, A. M. Korovin, S. M. Sutorin, D. A. Baranov, S. V. Gastev, B. B. Krichevstov, K. Y. Maksimova, A. I. Grunin, V. E. Bursian, L. V. Lutsev, and M. Tabuchi, Thin yttrium iron garnet films grown by pulsed laser deposition: Crystal structure, static, and dynamic magnetic properties, *J. Appl. Phys.* **119**, 023903 (2016).
- [33] L. Soumah, N. Beaulieu, L. Qassym, C. Carrétéro, E. Jacquet, R. Lebourgeois, J. Ben Youssef, P. Bortolotti, V. Cros, and A. Anane, Ultra-low damping insulating magnetic thin films get perpendicular, *Nat. Commun.* **9**, 3355 (2018).

- [34] E. R. Rosenberg, K. Litzius, J. M. Shaw, G. A. Riley, G. S. Beach, H. T. Nembach, and C. A. Ross, Magnetic properties and growth-induced anisotropy in yttrium thulium iron garnet thin films, *Adv. Electron. Mater.* **7**, 2100452 (2021).
- [35] H. Chang, P. A. P. Janantha, J. Ding, T. Liu, K. Cline, J. N. Gelfand, W. Li, M. C. Marconi, and M. Wu, Role of damping in spin Seebeck effect in yttrium iron garnet thin films, *Sci. Adv.* **3**, e1601614 (2017).
- [36] R. Kumar, B. Samantaray, and Z. Hossain, Ferromagnetic resonance studies of strain tuned Bi:YIG films, *J. Phys.: Condens. Matter* **31**, 435802 (2019).
- [37] S. Crossley, A. Quindeau, A. Swartz, E. Rosenberg, L. Beran, C. Avci, Y. Hikita, C. Ross, and H. Hwang, Ferromagnetic resonance of perpendicularly magnetized $\text{Tm}_3\text{Fe}_5\text{O}_{12}/\text{Pt}$ heterostructures, *Appl. Phys. Lett.* **115**, 172402 (2019).
- [38] R. Pearson, Magnetocrystalline anisotropy of rare-earth iron garnets, *J. Appl. Phys.* **33**, 1236 (1962).
- [39] S. Iida, Magnetostriction constants of rare earth iron garnets, *J. Phys. Soc. Jpn.* **22**, 1201 (1967).
- [40] C. Tang, P. Sellappan, Y. Liu, Y. Xu, J. E. Garay, and J. Shi, Anomalous Hall hysteresis in $\text{Tm}_3\text{Fe}_5\text{O}_{12}/\text{Pt}$ with strain-induced perpendicular magnetic anisotropy, *Phys. Rev. B* **94**, 140403(R) (2016).
- [41] A. Quindeau, C. O. Avci, W. Liu, C. Sun, M. Mann, A. S. Tang, M. C. Onbasli, D. Bono, P. M. Voyles, Y. Xu *et al.*, $\text{Tm}_3\text{Fe}_5\text{O}_{12}/\text{Pt}$ heterostructures with perpendicular magnetic anisotropy for spintronic applications, *Adv. Electron. Mater.* **3**, 1600376 (2017).
- [42] Y. Liu, H. Wong, K. Lam, K. Chan, C. Mak, and C. Leung, Anomalous Hall effect in $\text{Pt}/\text{Tb}_3\text{Fe}_5\text{O}_{12}$ heterostructure: Effect of compensation point, *J. Magn. Magn. Mater.* **468**, 235 (2018).
- [43] V. H. Ortiz, M. Aldosary, J. Li, Y. Xu, M. I. Lohmann, P. Sellappan, Y. Kodera, J. E. Garay, and J. Shi, Systematic control of strain-induced perpendicular magnetic anisotropy in epitaxial europium and terbium iron garnet thin films, *APL Mater.* **6**, 121113 (2018).
- [44] V. H. Ortiz, B. Arkook, J. Li, M. Aldosary, M. Biggerstaff, W. Yuan, C. Warren, Y. Kodera, J. E. Garay, I. Barsukov *et al.*, First- and second-order magnetic anisotropy and damping of europium iron garnet under high strain, *Phys. Rev. Mater.* **5**, 124414 (2021).
- [45] A. Mitra, O. Cespedes, Q. Ramasse, M. Ali, S. Marmion, M. Ward, R. Brydson, C. Kinane, J. Cooper, S. Langridge *et al.*, Interfacial origin of the magnetisation suppression of thin film yttrium iron garnet, *Sci. Rep.* **7**, 11774 (2017).
- [46] L. Caretta, E. Rosenberg, F. Büttner, T. Fakhru, P. Gargiani, M. Valvidares, Z. Chen, P. Reddy, D. A. Muller, C. A. Ross *et al.*, Interfacial Dzyaloshinskii-Moriya interaction arising from rare-earth orbital magnetism in insulating magnetic oxides, *Nat. Commun.* **11**, 1090 (2020).
- [47] R. Kumar, B. Samantaray, S. Das, K. Lal, D. Samal, and Z. Hossain, Damping in yttrium iron garnet films with interface, *Phys. Rev. B* **106**, 054405 (2022).